https://doi.org/10.15407/ujpe68.10.695

A.V. KOROTUN [1, 2]

[1] National University "Zaporizhzhya Polytechnic"
(64, Zhukovs'kogo Str., Zaporizhzhya 69063, Ukraine; e-mail: andko@zp.edu.ua)
[2] G.V. Kurdyumov Institute for Metal Physics, Nat. Acad. of Sci. of Ukraine
(36, Akademika Vernads'kogo Blvd., Kyiv 03142, Ukraine)

PLASMONIC PHENOMENA IN BICONICAL AND BIPYRAMIDAL METAL NANOPARTICLES

The optical characteristics of metal nanoparticles with biconical and bipyramidal shapes have been studied in the framework of the equivalent spheroid approach. The frequency dependences of the diagonal components of the polarizability tensor, the absorption and scattering cross-sections, and the frequencies of the longitudinal and transverse surface plasmon resonances are calculated for the particles with the indicated shapes. It is found that the position of the surface plasmon resonance significantly depends on the aspect ratio, if plasmon oscillations occur along the larger nanoparticle size, and it does not depend on the aspect ratio for plasmon oscillations along the smaller size. It is shown that the position and height of the maxima of the absorption cross-section depend not only on the aspect ratio, but also on the particle cross-section shape (a circle or a pentagon). In turn, a change in the nanoparticle material only shifts the spectrum curves, preserving the relative positions and magnitudes of the maxima of the absorption cross-sections.

K e y w o r d s: metal nanoparticle, bicone, bipyramid, plasmon resonance, polarizability, equivalent spheroid, aspect ratio.

1. Introduction

Plasmonic effects in the optical response of metal nanostructures have been widely studied experimentally and theoretically during the past several decades. This interest was stimulated by wide possibilities that those effects open for manipulating the optical properties of nanoparticles by changing their shape, size, structure, and composition [1–8]. This possibility arises due to the dependence of the frequencies of the localized surface plasmon resonance (SPR) on the nanoparticle morphology and the properties of the surrounding medium. Therefore, the SPR parameters can be adapted to specific applications [9]. This fact favored the development of new methods for synthesizing nano-objects of various shapes such as rods, bipyramids, bicones, dodecahedrons, triangles, cubes, and stars [10–16].

In contrast to spherical particles, prolate objects such as metal rods, due to their anisotropy, have two SPR peaks. However, along with attractive plasmonic properties, they also have some substantial drawbacks. In particular, flat ends of metal nanorods restrict the amplification of the local electric field by the nanorods, which weakens the signals of surface-enhanced Raman spectroscopy (SERS) [17]. Furthermore, metal nanorods obtained in nanoparticle ensembles under real conditions usually differ in their size and shape, which leads to a strong broadening of plasmon peaks. Therefore, an active search is contin-

C i t a t i o n: Korotun A.V. Plasmonic phenomena in biconical and bipyramidal metal nanoparticles. *Ukr. J. Phys.* **68**, No. 10, 695 (2023). https://doi.org/10.15407/ujpe68.10.695.
Ц и т у в а н н я: Коротун А.В. Плазмонні явища у біконічних і біпірамідальних металевих наночастинках. *Укр. фіз. журн.* **68**, №10, 697 (2023).

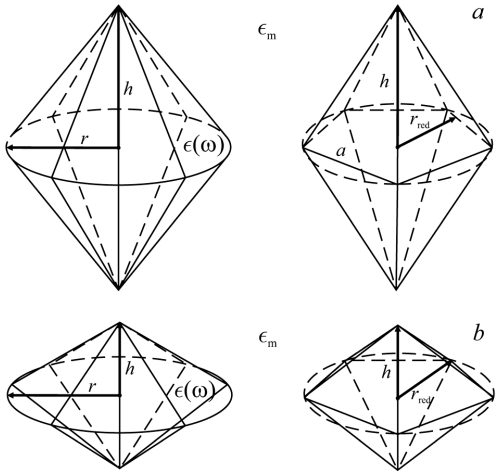

Fig. 1. Possible shapes of nanoparticles: prolate ($h > 2r$) bicone and bipyramid (a), oblate ($h < 2r$) bicone and bipyramid (b)

ued for such nanostructures that, together with preserving the useful plasmonic characteristics of metal rods, would be able to create a larger local field amplification, with their shape and dimensions being similar at that.

Examples of such nanostructures are metal bicones and bipyramids. A considerable surface-enhanced Raman scattering effect [18], a high sensitivity to the dielectric constant variation [19], the photothermal effect, and the photothermal stability are associated with the unique structure of bicones and bipyramids [20]. For instance, practically monodisperse metal bicones were obtained using the seeded growth method [21, 22]. In work [23], the possibility of detecting the biotin-streptavidin interaction in an active plasmonic nanoplatform using the LSPR and SERS methods was proved. The substantial amplification of the electric field at the tips of bicones (bipyramids) is also applied to monitor the enzyme-reagent interactions and conformational changes [24, 25]. Despite considerable efforts aimed at researching the properties of gold nanobicones and nanobipyramids [20, 23, 26–31], as well as their great importance for the biological monitoring, molecular imaging, tumor treatment, and other applications [27, 28, 31, 32], the issue of plasmonic properties of such nanoparticles remains poorly studied.

Therefore, the task of researching the optical phenomena in metal nanostructures with the biconical and bipyramidal shapes is challenging.

2. Theoretical Model

2.1. General relationships

Consider biconical and bipyramidal metal nanoparticles located in a medium with the dielectric constant ϵ_m (Fig. 1). Assume that the base of the bipyramid is a regular pentagon.

To study plasmonic phenomena in biconical and bipyramidal metal nanoparticles, let us apply the "equivalent-spheroid" approach, which was used in work [33] for rod-like nanoobjects. A basis for this approach to be applied consists in that the calculation results concerning the dependence of the longitudinal SPR frequency on the aspect ratio, i.e., the ratio between the transverse and longitudinal dimensions, obtained in the framework of this approach for metal cylinders agree quite well with the experimental ones. Therefore, to describe the plasmonic properties of bicones and bipyramids, we may use expressions for the diagonal components of the polarizability tensor of spheroids,

$$\alpha_{\perp(\parallel)}(\omega) = V \frac{\epsilon^{\perp(\parallel)}(\omega) - \epsilon_{\rm m}}{\epsilon_{\rm m} + \mathcal{L}_{\perp(\parallel)}\left[\epsilon^{\perp(\parallel)}(\omega) - \epsilon_{\rm m}\right]}, \tag{1}$$

where V is the volume of the equivalent spheroid, ω is the frequency of incident light, $\mathcal{L}_{\perp(\parallel)}$ are the depolarization factors of the spheroid, and the expressions for the diagonal components of the dielectric tensor of the particle material in the Drude model look like

$$\epsilon^{\perp(\parallel)}(\omega) = \epsilon^{\infty} - \frac{\omega_p^2}{\omega\left(\omega + i\gamma_{\rm eff}^{\perp(\parallel)}\right)}. \tag{2}$$

In formulas (2), ϵ^{∞} is the contribution of the crystal lattice to the dielectric function, ω_p is the plasma frequency, and the effective relaxation rate $\gamma_{\rm eff}^{\perp(\parallel)}$ is determined by the additive contributions of the rates of the bulk, $\gamma_{\rm bulk}$, and surface, $\gamma_{\rm s}^{\perp(\parallel)}$, relaxations and the radiative attenuation, $\gamma_{\rm rad}^{\perp(\parallel)}$, as follows:

$$\gamma_{\rm eff}^{\perp(\parallel)} = \gamma_{\rm bulk} + \gamma_{\rm s}^{\perp(\parallel)} + \gamma_{\rm rad}^{\perp(\parallel)}. \tag{3}$$

If the bulk relaxation rate $\gamma_{\rm bulk}$ is constant, then $\gamma_{\rm s}^{\perp(\parallel)}$ and $\gamma_{\rm rad}^{\perp(\parallel)}$ are determined by the formulas [33]

$$\gamma_{\rm s}^{\perp(\parallel)} = \frac{\mathcal{L}_{\perp(\parallel)}\sigma_{\perp(\parallel)}}{\epsilon_0\left[\epsilon_{\rm m} + \mathcal{L}_{\perp}(1 - \epsilon_{\rm m})\right]}, \tag{4}$$

$$\gamma_{\rm rad}^{\perp(\parallel)} = \frac{2V}{9\pi\epsilon_0}\left(\frac{\omega_p}{c}\right)^3 \frac{\mathcal{L}_{\perp(\parallel)}\sigma_{\perp(\parallel)}}{\sqrt{\epsilon_{\rm m}\left[\epsilon^{\infty} + \frac{1-\mathcal{L}_{\perp(\parallel)}}{\mathcal{L}_{\perp(\parallel)}}\epsilon_{\rm m}\right]}}, \tag{5}$$

where ϵ_0 is the electric constant, c is the speed of light, and $\sigma_{\perp(\parallel)}$ are the diagonal components of the conductivity tensor of the spheroid.

Note that two fundamentally different situations are possible for nanoparticles with the examined shapes: (i) $h > 2r$, where r is the radius of the bicone base or the reduced radius of the bipyramid base, and h is the bicone or bipyramid height (Fig. 1, *a*), and (ii) $h < 2r$ (Fig. 1, *b*). An equivalent spheroid is prolate in the former case, and oblate in the latter one.

The reduced radius of the bipyramid base can be found from the condition that the base areas of the bipyramid and the bicone are identical,

$$S_{\rm bic} = S_{\rm bip}, \tag{6}$$

whence

$$S_{\rm bic} = \pi r^2, \quad S_{\rm bip} = \frac{5r_{\rm red}^2}{4}\cot\frac{\pi}{5}, \tag{7}$$

where

$$r_{\rm red} = r\sqrt{\frac{4\pi}{5\,\cot\,\frac{\pi}{5}}} \approx 1.35r. \tag{8}$$

In what follows, the expressions for the depolarization factors and the diagonal components of the conductivity tensor will be given separately for each case.

2.2. Bicone and bipyramid with $h > 2r$. Equivalent prolate spheroid

The formulas for the depolarization factors $\mathcal{L}_{\parallel(\perp)}$ and the diagonal components of the conductivity tensor $\sigma_{\perp(\parallel)}$ of a prolate spheroid were obtained in work [33]:

$$\mathcal{L}_{\parallel} = \frac{\varrho_{\rm eff}^2}{1-\varrho_{\rm eff}^2}\left(\frac{1}{2\sqrt{1-\varrho_{\rm eff}^2}}\ln\frac{1+\sqrt{1-\varrho_{\rm eff}^2}}{1-\sqrt{1-\varrho_{\rm eff}^2}} - 1\right), \tag{9}$$

$$\mathcal{L}_{\perp} = \frac{1}{2}\left(1-\mathcal{L}_{\parallel}\right), \tag{10}$$

$$\sigma_{\perp(\parallel)}(\omega) = \frac{9}{16}\epsilon_0\left(\frac{\omega_p}{\omega}\right)^2\nu_{s,\perp}\mathscr{F}_{\perp(\parallel)}(\varrho_{\rm eff}). \tag{11}$$

In formula (11), $\nu_{s,\perp} = v_{\rm F}/2r$ is the frequency of transverse oscillations ($v_{\rm F}$ is the Fermi velocity), $\varrho_{\rm eff}$ is the effective aspect ratio, and the size-dependent functions $\mathscr{F}_{\perp(\parallel)}(\varrho_{\rm eff})$ are determined by the expressions

$$\mathscr{F}_{\perp}(\varrho_{\rm eff}) = \left(1-\varrho_{\rm eff}^2\right)^{-\frac{3}{2}} \times$$

$$\times\left\{\varrho_{\rm eff}\left(\frac{3}{2}-\varrho_{\rm eff}^2\right)\sqrt{1-\varrho_{\rm eff}^2} + 2\left(\frac{3}{4}-\varrho_{\rm eff}^2\right)\left(\frac{\pi}{2}-\arcsin\varrho_{\rm eff}\right)\right\}; \tag{12}$$

$$\mathscr{F}_{\parallel}(\varrho_{\rm eff}) = \left(1-\varrho_{\rm eff}^2\right)^{-\frac{3}{2}} \times$$

$$\times\left\{\frac{\pi}{2}-\arcsin\varrho_{\rm eff}+\varrho_{\rm eff}\left(1-2\varrho_{\rm eff}^2\right)\sqrt{1-\varrho_{\rm eff}^2}\right\}. \tag{13}$$

2.3. Bicone and bipyramid with $h < 2r$. Equivalent oblate spheroid

The depolarization factors of an oblate spheroid are determined by the formulas [34]

$$\mathcal{L}_{\parallel} = \frac{\varrho_{\rm eff}^2}{\left(\varrho_{\rm eff}^2-1\right)^{3/2}}\left(\sqrt{\varrho_{\rm eff}^2-1} - \operatorname{arctg}\sqrt{\varrho_{\rm eff}^2-1}\right), \tag{14}$$

$$\mathcal{L}_{\perp} = \frac{1}{2}\left(1-\mathcal{L}_{\parallel}\right), \tag{15}$$

The form of the corresponding expressions for $\sigma_{\perp(\parallel)}(\omega)$ coincides with that of expressions (11), but with other formulas for the size-dependent functions $\mathscr{F}_{\perp(\parallel)}(\varrho_{\rm eff})$ [34]:

$$\mathscr{F}_{\perp}(\varrho_{\rm eff}) = \frac{1}{2}\left(\varrho_{\rm eff}^2-1\right)^{-\frac{3}{2}} \times$$

$$\times\left\{\varrho_{\rm eff}\left(2\varrho_{\rm eff}^2-3\right)\sqrt{\varrho_{\rm eff}^2-1} + \left(4\varrho_{\rm eff}^2-3\right)\ln\left(\varrho_{\rm eff}+\sqrt{\varrho_{\rm eff}^2-1}\right)\right\}, \tag{16}$$

$$\mathscr{F}_{\parallel}(\varrho_{\rm eff}) = \left(\varrho_{\rm eff}^2-1\right)^{-\frac{3}{2}}\left\{\varrho_{\rm eff}\left(2\varrho_{\rm eff}^2-1\right)\sqrt{\varrho_{\rm eff}^2-1} - \ln\left(\varrho_{\rm eff}+\sqrt{\varrho_{\rm eff}^2-1}\right)\right\}. \tag{17}$$

Hence, the formulas for the surface relaxation and radiative attenuation rates have the following forms that are identical in both cases:

$$\gamma_{\rm s}^{\perp(\parallel)} = \frac{9}{16}\frac{\mathcal{L}_{\perp(\parallel)}}{\epsilon_{\rm m}+\mathcal{L}_{\perp(\parallel)}\left(1-\epsilon_{\rm m}\right)}\nu_{s,\perp}\left(\frac{\omega_p}{\omega}\right)\mathscr{F}_{\perp(\parallel)}(\varrho_{\rm eff}); \tag{18}$$

$$\gamma_{\rm rad}^{\perp(\parallel)} = \frac{V}{8\pi}\frac{\mathcal{L}_{\perp(\parallel)}}{\sqrt{\epsilon_{\rm m}\left(\epsilon^{\infty}+\frac{1-\mathcal{L}_{\perp(\parallel)}}{\mathcal{L}_{\perp(\parallel)}}\epsilon_{\rm m}\right)}} \times$$

$$\times\,\nu_{s,\perp}\left(\frac{\omega_p}{c}\right)^3\left(\frac{\omega_p}{\omega}\right)^2\mathscr{F}_{\perp(\parallel)}(\varrho_{\rm eff}). \tag{19}$$

2.4. Effective aspect ratio

The effective aspect ratio is determined from the equality of the ratios between the corresponding axial moments of inertia for the bicones (bipyramids) and the equivalent prolate (oblate) spheroids.

The axial moments of inertia for bicones (bipyramids) are determined by the expressions

$$I_x = 2m\left(\frac{3}{20}r^2 + \frac{1}{10}h^2\right) = \frac{1}{5}m\left(\frac{3}{2}r^2 + h^2\right),$$
$$I_z = \frac{3}{5}mr^2. \tag{20}$$

Whence we obtain

$$\frac{I_x}{I_z} = \frac{1}{2} + \frac{1}{3\varrho^2}, \tag{21}$$

where

$$\varrho = \frac{r}{h} \tag{22}$$

is the aspect ratio for the bicones (bipyramids) in both examined cases.

For the equivalent prolate spheroids,

$$I_x = \frac{1}{5}m\left(a^2 + b^2\right), \quad I_z = \frac{2}{5}mb^2, \tag{23}$$

where a and b are the major and minor semiaxes, respectively. Therefore,

$$\frac{I_x}{I_z} = \frac{1}{2} + \frac{1}{2\varrho_{\text{eff}}^2}, \tag{24}$$

where

$$\varrho_{\text{eff}} = \frac{b}{a} \tag{25}$$

is the effective aspect ratio.

For the equivalent oblate spheroids,

$$I_x = \frac{1}{5}m\left(a^2 + b^2\right), \quad I_z = \frac{2}{5}ma^2. \tag{26}$$

Since now the effective aspect ratio equals

$$\varrho_{\text{eff}} = \frac{a}{b}, \tag{27}$$

then the expression for I_x/I_z coincides with formula (24).

Equating formulas (21) and (24), we obtain the following relation between the aspect and effective aspect ratios:

$$\varrho_{\text{eff}} = \sqrt{\frac{3}{2}}\varrho. \tag{28}$$

3. Calculation Results and Their Discussion

The frequency dependences of the diagonal components of the polarizability tensor, as well as the absorption and scattering cross-sections, were calculated for the bicones and bipyramids with various sizes and compositions. The parameters of the metals are quoted in Table 1.

In Fig. 2, the frequency dependences of the real and imaginary parts and the absolute values of the longitudinal and transverse components of the polarizability tensor calculated for the bicones and bipyramids with $h > 2r$ are shown. It should be noted that the results of calculations of Re $\alpha_\perp$, Im $\alpha_\perp$, and $|\alpha_\perp|$ for the bicones and bipyramids are slightly different, whereas the maxima of Im $\alpha_\perp$ (i.e., for the transverse SPR) are reached at the same frequencies, $\omega_{sp}^{\perp\,\text{bc}} = \omega_{sp}^{\perp\,\text{bp}}$.

At the same time, the frequency of the longitudinal SPR for the bipyramids is higher than that for the bicones. The maxima of Re $\alpha_\parallel(\hbar\omega)$ and $|\alpha_\parallel(\hbar\omega)|$ have the same relative positions.

In the case of bicones and bipyramids with $h < 2r$ (Fig. 3), the situation is opposite: the results for Re $\alpha_\parallel$, Im $\alpha_\parallel$, and $|\alpha_\parallel|$ practically coincide, $\omega_{sp}^{\parallel\,\text{bc}} = \omega_{sp}^{\parallel\,\text{bp}}$, whereas the frequencies of the transverse SPR are different (for the bicones, they are higher than for the bipyramids). In addition, if $\max\{\text{Im }\alpha_\parallel^{\text{bc}}\} < \max\{\text{Im }\alpha_\parallel^{\text{bp}}\}$, then $\max\{\text{Im }\alpha_\perp^{\text{bc}}\} < \max\{\text{Im }\alpha_\perp^{\text{bp}}\}$.

The results of calculations obtained for the frequency dependences of the absorption, C_{abs}, and scattering, C_{sca}, cross-sections of the bicones and bipyramids with $h > 2r$ and $h < 2r$ are shown in Figs. 4 and 5, respectively.

Each of those dependences has two maxima corresponding to the longitudinal and transverse SPRs, except for the case of $C_{\text{sca}}(\hbar\omega)$ for the bicones and

Table 1. **Parameters of metals (see, e.g., [34, 35] and references therein)**

Parameter	Al	Cu	Au	Ag	Pt	Pd
r_s/a_0	2.07	2.11	3.01	3.02	3.27	4.00
m^*/m_e	1.06	1.49	0.99	0.96	0.54	0.37
ϵ^∞	0.7	12.03	9.84	3.7	4.42	2.52
τ_{bulk}, fs	8	27	29	40	9.5	7.2

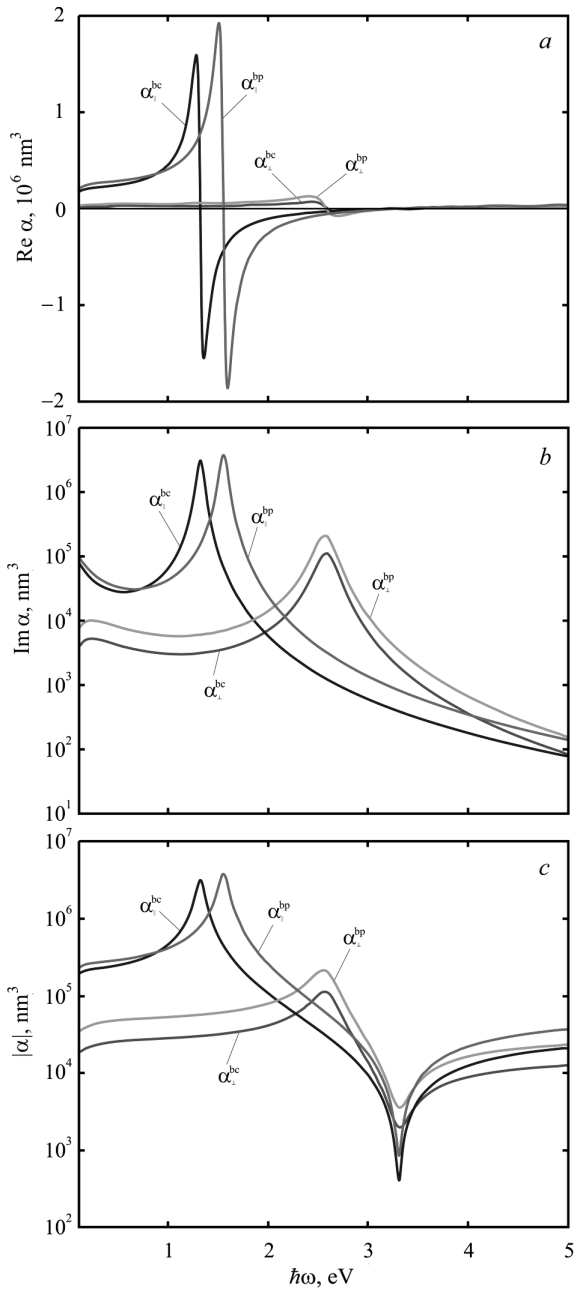

Fig. 2. Frequency dependences of the real (a) and imaginary (b) parts and the absolute value (c) of the longitudinal and transverse components of the polarizability of the prolate ($r = 10$ nm, $h = 60$ nm) biconical and bipyramidal gold particles

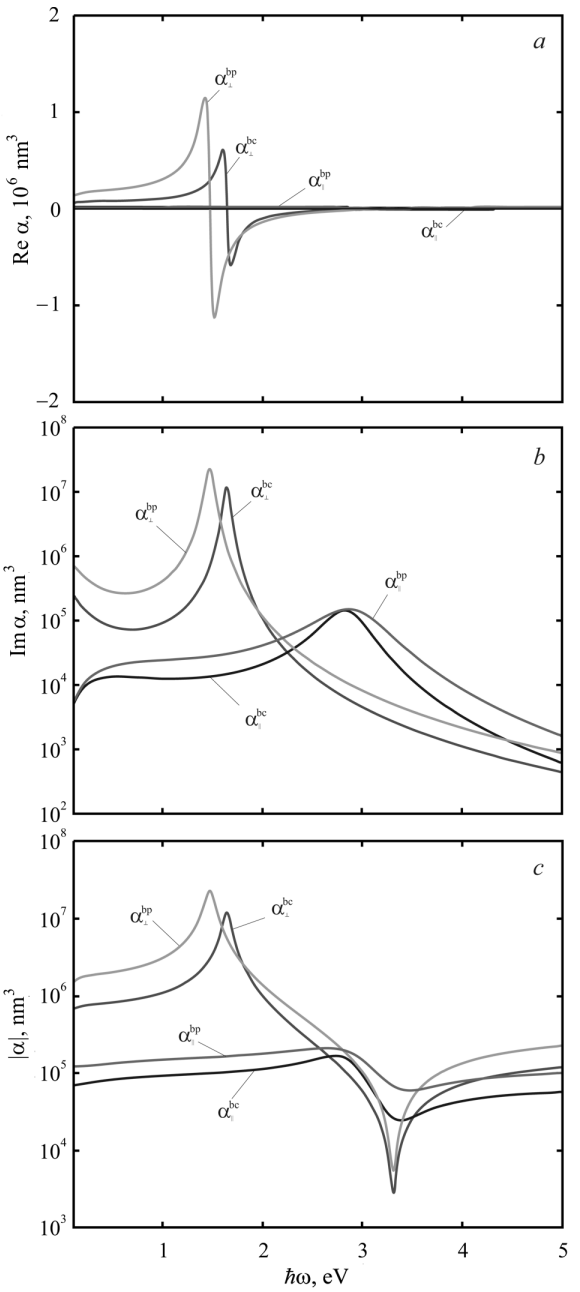

Fig. 3. Frequency dependences of the real (a) and imaginary (b) parts and the absolute value (c) of the longitudinal and transverse components of the polarizability of the oblate ($r = 60$ nm, $h = 10$ nm) biconical and bipyramidal gold particles

bipyramids with $h < 2r$. The latter occurs, because the second maximum of $C_{\rm sca}^{\rm bc(bp)}$ disappears at the given value of the aspect ratio. Note that such parameters of $\max\{C_{\rm abs}^{\rm bc(bp)}, C_{\rm sca}^{\rm bc(bp)}\}$ as the position and the relative magnitude behave themselves similarly to $\max\{\mathrm{Im}\ \alpha_{\perp}^{\rm bc(bp)}, \mathrm{Im}\ \alpha_{\parallel}^{\rm bc(bp)}\}$.

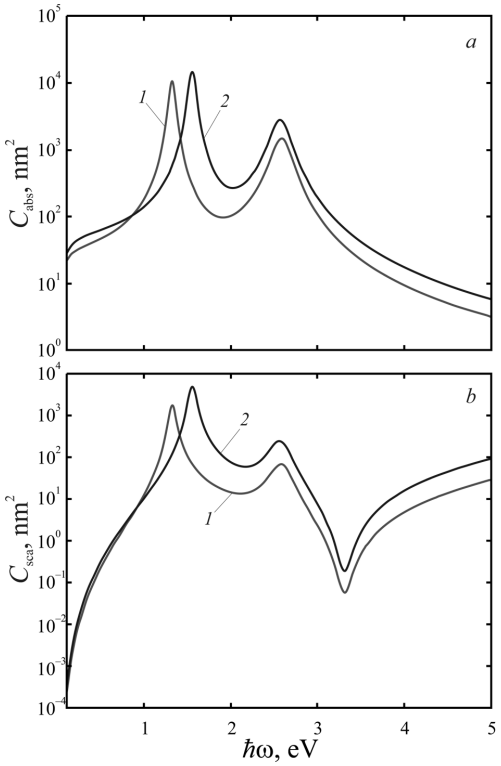

Fig. 4. Frequency dependences of the absorption (a) and scattering (b) cross-sections for the prolate (r = 10 nm, h = 60 nm) biconical (curves *1*) and bipyramidal (curves *2*) gold particles

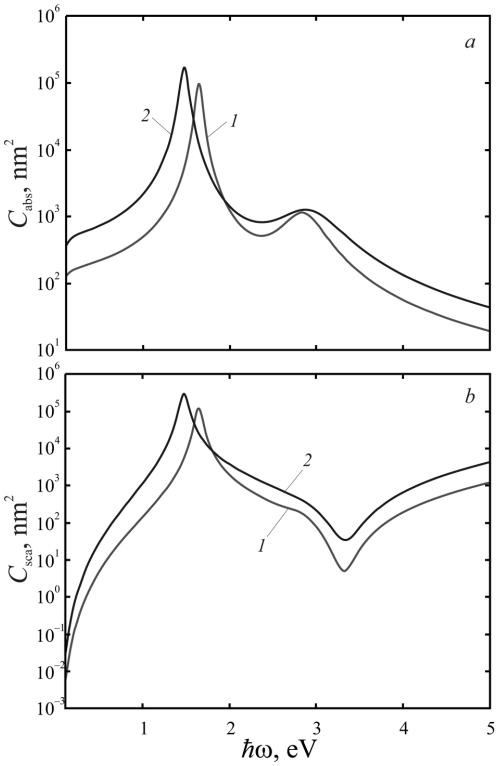

Fig. 5. Frequency dependences of the absorption (a) and scattering (b) cross-sections for the oblate (r = 60 nm, h = = 10 nm) biconical (curves *1*) and bipyramidal (curves *2*) gold particles

Table 2. **Calculated SER frequencies for a prolate bicone**

ϱ	Au		Cu	
	$\omega_{sp}^{\perp}$, eV	$\omega_{sp}^{\parallel}$, eV	$\omega_{sp}^{\perp}$, eV	$\omega_{sp}^{\parallel}$, eV
0.05	2.598	0.570	3.322	0.788
0.10	2.589	0.951	3.312	1.305
0.15	2.578	1.235	3.300	1.682
0.20	2.565	1.455	3.286	1.966
0.25	2.551	1.628	3.271	2.185
0.30	2.537	1.767	3.256	2.358
0.35	2.523	1.881	3.240	2.497
0.40	2.508	1.975	3.224	2.611
0.45	2.493	2.054	3.207	2.705
0.50	2.478	2.122	3.191	2.785
0.55	2.463	2.180	3.175	2.852
0.60	2.449	2.230	3.158	2.910
0.65	2.434	2.274	3.142	2.961
0.70	2.420	2.313	3.126	3.005
0.75	2.406	2.347	3.110	3.044
0.80	2.391	2.377	3.094	3.078

Table 3. **Calculated SER frequencies for an oblate bicone**

ϱ	Au		Cu	
	$\omega_{sp}^{\perp}$, eV	$\omega_{sp}^{\parallel}$, eV	$\omega_{sp}^{\perp}$, eV	$\omega_{sp}^{\parallel}$, eV
1.05	1.856	2.766	2.467	3.501
1.10	2.165	2.640	2.835	3.367
1.15	2.288	2.533	2.977	3.251
1.20	2.348	2.454	3.045	3.164
1.25	2.378	2.403	3.079	3.107
1.30	2.391	2.376	3.094	3.076
1.35	2.396	2.367	3.099	3.066
1.40	2.394	2.370	3.097	3.070
1.45	2.389	2.382	3.091	3.083
1.50	2.381	2.398	3.082	3.101
1.55	2.371	2.416	3.071	3.121
1.60	2.360	2.435	3.058	3.142
1.65	2.348	2.454	3.045	3.164
1.70	2.336	2.472	3.031	3.184
1.75	2.323	2.490	3.017	3.204
1.80	2.311	2.507	3.003	3.222

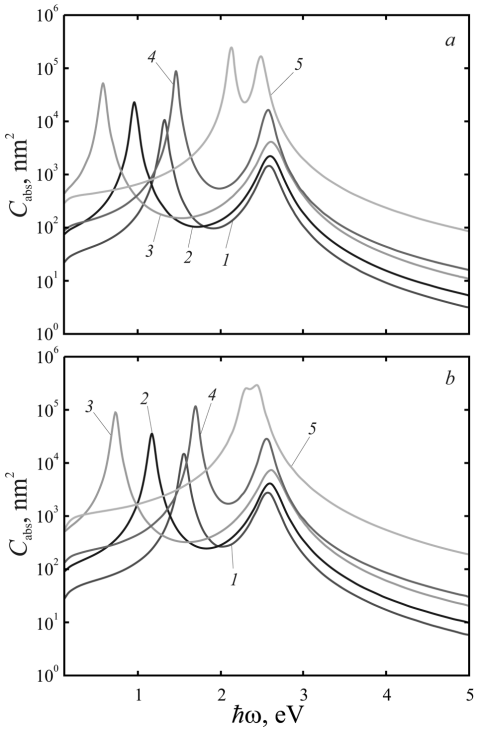

Fig. 6. Frequency dependences of the absorption cross-sections for the biconical (a) and bipyramidal (b) gold particles: r = 10 nm, h = 60 nm (*1*); r = 10 nm, h = 100 nm (*2*); r = 10 nm, h = 200 nm (*3*); r = 20 nm, h = 100 nm (*4*); r = 50 nm, h = 100 nm (*5*)

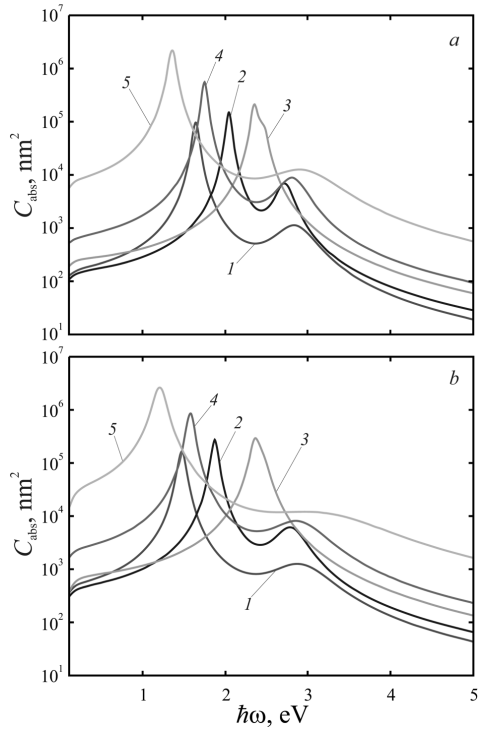

Fig. 7. Frequency dependences of the absorption cross-sections for the biconical (a) and bipyramidal (b) gold particles: r = 60 nm, h = 10 nm (*1*); r = 60 nm (*2*), h = 20 nm; r = 60 nm, h = 50 nm (*3*); r = 100 nm, h = 20 nm (*4*); r = 200 nm, h = 20 nm (*5*)

Figures 6 and 7 demonstrate the frequency dependences of the absorption cross-sections for the bicones and bipyramids with various aspect ratios. Note that, in the case of particles with $h > 2r$ (Fig. 6), the distance between the maxima decreases as the aspect ratio increases, and, for each aspect ratio value, the distance between the maxima is always smaller for the bipyramidal nanoparticles. In the case of particles with $h < 2r$ (Fig. 7), the distance between the maxima of the absorption cross-sections is smaller than in the case $h > 2r$, the magnitude of the second maximum is substantially smaller than the magnitude of the first maximum, and, as the aspect ratio increases, the magnitude of the second maximum decreases until it disappears completely.

The described behavior of the maxima in the absorption cross-sections of the bicones with $h > 2r$ and $h < 2r$ is confirmed by the calculations of the frequencies of the transverse and longitudinal SPRs (Tables 2 and 3). In particular, the inequality $\omega_{sp}^{\parallel} < \omega_{sp}^{\perp}$ always holds for the nanoparticles with $h > 2r$, and the inverse inequality $\omega_{sp}^{\parallel} > \omega_{sp}^{\perp}$ always holds for the nanoparticles with $h < 2r$. It should also be noted that, as the effective aspect ratio of the particles with $h > 2r$ increases, the maxima in the absorption cross-section "attract" each other (i.e., the frequency splitting value $\Delta\omega_{sp} = \omega_{sp}^{\perp} - \omega_{sp}^{\parallel}$ diminishes). At the same time, for the particles with $h < 2r$, the opposite effect takes place: as the effective aspect ratio increases, those maxima "repulse" each other, and the frequency splitting value $\Delta\omega_{sp} = \omega_{sp}^{\parallel} - \omega_{sp}^{\perp}$ increases. This occurs, because if ϱ_{eff} decreases in the case $h > 2r$ or increases in the case $h < 2r$, the shape of the equivalent spheroid more and more deviates from the spherical one.

The frequency dependences of the absorption cross-sections of the bicones and bipyramids made of various metals are shown in Figs. 8 and 9. Note that, for the nanoparticles with $h > 2r$ the maxima of the absorption cross-sections corresponding to the longi-

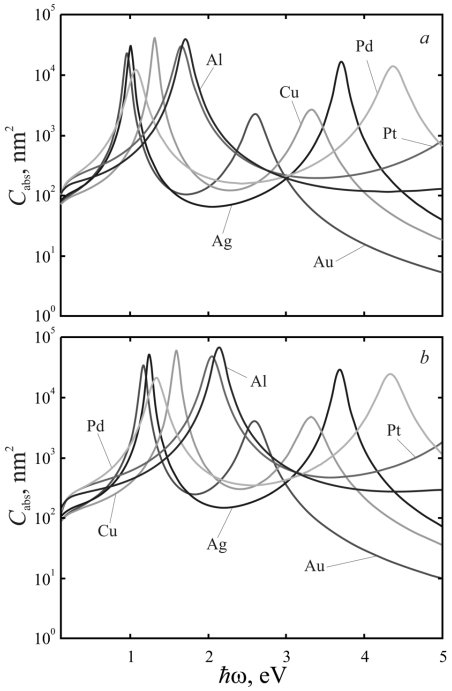

Fig. 8. Frequency dependences of absorption cross-sections for the prolate (r = 10 nm, h = 100 nm) biconical (a) and bipyramidal (b) particles of various metals

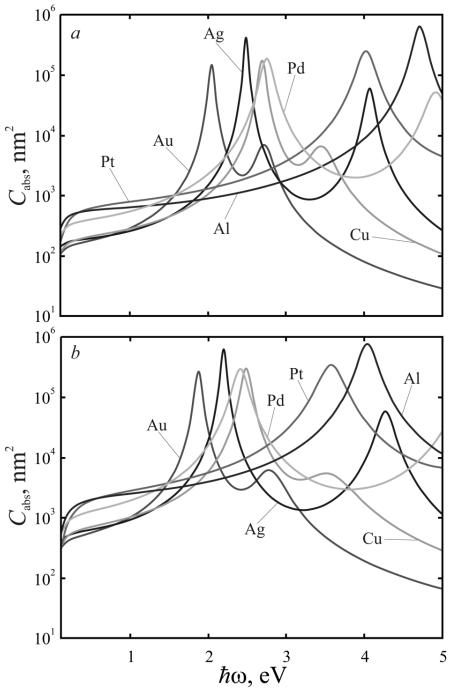

Fig. 9. Frequency dependences of absorption cross sections for the oblate (r = 60 nm, h = 20 nm) biconical (a) and bipyramidal (b) particles of various metals

tudinal SPR in the bipyramids are reached at higher frequencies than in the case of bicones, whereas their transverse SPR frequencies are identical. In the case of the bicones and bipyramids with $h < 2r$, the situation is opposite: the longitudinal SPR frequencies for the bicones and bipyramids coincide, whereas the transverse SPR frequencies for the bicones are higher than for the bipyramids. The $C_{\rm abs}\,(\hbar\omega)$ curves for different metals are shifted with respect to one another, because the bulk plasmon frequencies in them are different, and, as a result, the frequencies of the longitudinal and transverse SPRs are also different.

4. Conclusions

To summarize, the size and frequency dependences of the diagonal components of the polarizability tensor and the absorption and scattering cross-sections of nano-sized bicones and bipyramids have been calculated. The results of calculations of the frequency dependences of the diagonal polarizability components of the bicones and bipyramids, when their heights are larger than their diameters (reduced diameters), testify that the real and imaginary parts and the absolute value of the transverse component of the polarizability tensor of the bicones and bipyramids are practically identical, and the transverse surface plasmon resonance is excited at the same frequencies. In turn, the frequency of the longitudinal SPR for the bipyramids in this case is higher than for the bicones. In the case of the bicones and bipyramids, whose height is smaller than the diameter, the frequency dependences of the real and imaginary parts and the absolute value of the longitudinal component of the polarizability tensor for the particles of both forms are practically identical, whereas the transverse SPR frequencies are different, being higher for the bicones.

The frequency dependences of absorption and scattering cross-sections for the particles with the studied shapes and any ratio between their height and diameter are found to have two maxima each, except for the scattering cross-section for the bicones and bipyramids with the height smaller than the diameter for some values of the aspect ratio, when the second maximum disappears

It is shown that if the bicone (bipyramid) height exceeds the diameter, the distance between the maxima decreases, as the aspect ratio increases, with the distance between the maxima for the biconical parti-

cles being always larger than for the bipyramidal ones at any aspect ratio. At the same time, in contrast to the previous case, for the particles of all examined forms with the height smaller than the diameter, the distance between the maxima in the absorption cross-section is larger, and the magnitude of the second maximum is substantially smaller than that of the first maximum and, as the aspect ratio grows, decreases until its complete disappearance.

It is proved that the positions of the maxima in the absorption cross-sections correspond to the calculated values of the transverse and longitudinal SPR frequencies. The more the shape of the equivalent spheroid differs from the spherical one, the larger the difference between those frequencies.

All specific features in the frequency dependences of the absorption cross-sections for the biconical and bipyramidal gold nanoparticles are found to survive in the corresponding dependences for the nanoparticles of other metals. The only difference consists in a relevant shift of the spectrum because of different bulk plasmon frequencies.

1. U. Kreibig, M. Vollmer. *Optical Properties of Metal Clusters* (Springer, 1995) [ISBN: 978-3-662-09109-8].
2. F. Vallée. In: *Nanomaterials and Nanochemistry.* Edited by C. Bréchignac, P. Houdy, M. Lahmani (Springer, 2007) [ISBN: 978-3-540-72992-1].
3. K.A. Willets, R.P. Van Duyne. Localized surface plasmon resonance spectroscopy and sensing. *Annu. Rev. Phys. Chem.* **58**, 267 (2007).
4. S.A. Maier. *Plasmonics: Fundamentals and Applications* (Springer, 2007) [ISBN: 978-0-387-37825-1].
5. M.L. Dmytruk, S.Z. Malynych. Surface plasmon resonances and their manifestation in the optical properties of noble metal nanostructures. *Ukr. Fiz. Zh. Ogl.* **9**, 3 (2014) [in Ukrainian].
6. D.J. De Aberasturi, A.B. Serrano-Montes, L.M. Liz-Marzán. Modern applications of plasmonic nanoparticles: From energy to health. *Adv. Opt. Mater.* **3**, 602 (2015).
7. *Handbook of Surface Plasmon Resonance.* Edited by R.B.M. Schasfoort (RSC Publishing, 2017) [ISBN: 978-1-78262-730-2].
8. A.O. Koval, A.V. Korotun, Yu.A. Kunytskyi, V.A. Tatarenko, I.M. Titov. *Electrodynamics of Plasmonic Effects in Nanomaterials* (Naukova Dumka, 2021) [in Ukrainian] [ISBN: 978-966-00-1761-0].
9. N.I. Grigorchuk, P.M. Tomchuk. Cross-sections of electric and magnetic light absorption by spherical metallic nanoparticles. The exact kinetic solution. *Ukr. J. Phys.* **51**, 921 (2006).
10. L.M. Liz-Marzan. Tailoring surface plasmons through the morphology and assembly of metal nanoparticles. *Langmuir* **22**, 32 (2006).
11. C.J. Murphy, N.R. Jana. Controlling the aspect ratio of inorganic nanorods and nanowires. *Adv. Mater.* **14**, 80 (2002).
12. X.C. Jiang, M.P. Pileni. Gold nanorods: influence of various parameters as seeds, solvent, surfactant on shape control. *Colloid. Surf. A* **295**, 228 (2007).
13. M. Liu, P.J. Guyot-Sionnest. Mechanism of silver(i) – Assisted growth of gold nanorods and bipyramids. *J. Phys. Chem. B* **109**, 22192 (2005).
14. L.J. Sherry, S.H. Chang, G.C. Schatz, R.P. Van Duyne, B.J. Wiley, B.J. Xia. Localized surface plasmon resonance spectroscopy of single silver nanocubes. *Nano Lett.* **5**, 2034 (2005).
15. J. Rodriguez-Fernandez, C. Novo, V. Myroshnychenko, A.M. Funston, A. Sánchez-Iglesias, I. Pastoriza-Santos, J. Pérez-Juste, F. Javier Garcia de Abajo, L.M. Liz-Marzán, P. Mulvaney. Spectroscopy, imaging, and modeling of individual gold decahedra. *J. Phys. Chem. C* **113**, 18623 (2009).
16. C.L. Nehl, H. Liao, J.H. Hafner. Optical properties of star-shaped gold nanoparticles. *Nano Lett.* **6**, 683 (2006).
17. S. Xu, L. Jiang, Y. Nie, J. Wang, H. Li, Y. Liu, W. Wang, G. Xu, X. Luo. Gold nanobipyramids as dual-functional substrates for in situ "Turn on" analyzing intracellular telomerase activity based on target-triggered plasmon-enhanced fluorescence. *ACS Appl. Mater. Inter.* **10**, 26851 (2018).
18. F. Zhao, X. Wang, Y. Zhang, X. Lu, H. Xie, B. Xu, W. Ye, W. Ni. In situ monitoring of silver adsorption on assembled gold nanorods by surface-enhanced Raman scattering. *Nanotechnology* **31**, 295601 (2020).
19. Q. Li, X. Zhuo, S. Li, Q. Ruan, Q.-H. Xu, J. Wang. Production of monodisperse gold nanobipyramids with number percentages approaching 100% and evaluation of their plasmonic properties. *Adv. Opt. Mater.* **3**, 801 (2015).
20. T.H. Chow, N. Li, X. Bai, X. Zhuo, L. Shao, J. Wang. Gold nanobipyramids: an emerging and versatile type of plasmonic nanoparticles. *Acc. Chem. Res.* **52**, 2136 (2019).
21. D. Chateau, A. Liotta, F. Vadcard, J.R. Navarro, F. Chaput, J. Lerme, F. Lerouge, S. Parola. From gold nanobipyramids to nanojavelins for a precise tuning of the plasmon resonance to the infrared wavelengths: experimental and theoretical aspects. *Nanoscale* **7**, 1934 (2015).
22. A. Sánchez-Iglesias, N. Winckelmans, T. Altantzis, S. Bals, M. Grzelczak, L.M. Liz-Marzán. High-yield seeded growth of monodisperse pentatwinned gold nanoparticles through thermally induced seed twinning. *J. Am. Chem. Soc.* **139**, 107 (2017).
23. S. Nafisah, M. Morsin, N.A. Jumadi, N. Nayan, N.S.M. Shah, N.L. Razali, N.Z. Anrnisa. Improved sensitivity and selectivity of direct localized surface plasmon resonance sensor using gold nanobipyramids for glyphosate detection. *IEEE Sens. J.* **20**, 2378 (2019).

24. J.R. Mejia-Salazar, O.N. Oliveira Jr. Plasmonic biosensing. *Chem. Rev.* **118**, 10617 (2018).
25. E. Kim, M.D. Baaske, I. Schuldes, P.S. Wilsch, F. Vollmer. Label-free optical detection of single enzyme-reactant reactions and associated conformational changes. *Sci. Adv.* **3**, e1603044 (2017).
26. Y. Kang, H.-X. Gu, X. Zhang. A self-referenced method for determination of patulin by surface-enhanced Raman scattering using gold nanobipyramids as the substrate. *Anal. Methods* **11**, 5142 (2019).
27. Y. Lin, P. Kannan, Y. Zeng, B. Qiu, L. Guo, Z. Lin. Enzyme-free multicolor biosensor based on Cu^{2+}-modified carbon nitride nanosheets and gold nanobipyramids for sensitive detection of neuron specific enolase. *Sensor. Actuat. B Chem.* **283**, 138 (2019).
28. H. Mei, X. Wang, T. Zeng, L. Huang, Q. Wang, D. Ru, T. Huang, F. Tian, H. Wu, J. Gao. A nanocomposite consisting of gold nanobipyramids and multiwalled carbon nanotubes for amperometric nonenzymatic sensing of glucose and hydrogen peroxide. *Microchim. Acta* **186**, 235 (2019).
29. S. Xu, L. Jiang, Y. Liu, P. Liu, W. Wang, X. Luo. A morphology-based ultrasensitive multicolor colorimetric assay for detection of blood glucose by enzymatic etching of plasmonic gold nanobipyramids. *Anal. Chim. Acta* **1071**, 53 (2019).
30. X.L. Zhuo, X.Z. Zhu, Q. Li, Z. Yang, J.F. Wang. Gold nanobipyramid-directed growth of Length-Variable Silver Nanorods with multipolar plasmon resonances. *ACS Nano* **9**, 7523 (2015).
31. J. Feng, L. Chen, Y. Xia, J. Xing, Z. Li, Q. Qian, Y. Wang, A. Wu, L. Zeng, Y. Zhou. Bioconjugation of gold nanobipyramids for SERS detection and targeted photothermal therapy in breast Cancer. *ACS Biomater. Sci. Eng.* **3**, 608 (2017).
32. Z. Chu, H. Zhang, Y. Wu, C. Zhang, J. Liu, J. Yang. Passively Q-switched laser based on gold nanobipyramids as saturable absorbers in the 1.3 μm region. *Opt. Commun.* **406**, 209 (2018).
33. A.V. Korotun, Y.V. Karandas, V.I. Reva. Analytical theory of plasmon effects in rod-like metal nanoparticles. The equivalent-spheroid model *Ukr. J. Phys.* **67**, 849 (2022).
34. A.V. Korotun, N.I. Pavlyshche. Optical absorption of a composite with randomly distributed metallic inclusions of various shapes. *Funct. Mater.* **29**, 567 (2022).
35. A.V. Korotun, Ya.V. Karandas. Surface plasmons in a nanotube with a finite-thickness wall. *Phys. Metal. Metallogr.* **123**, 7 (2022).

Received 06.08.23.
Translated from Ukrainian by O.I. Voitenko

А.В. Коротун

ПЛАЗМОННІ ЯВИЩА
У БІКОНІЧНИХ І БІПІРАМІДАЛЬНИХ
МЕТАЛЕВИХ НАНОЧАСТИНКАХ

В роботі в рамках підходу еквівалентного сфероїда досліджуються оптичні характеристики металевих наночастинок біконічної та біпірамідальної форм. Проведено розрахунки частотних залежностей діагональних компонент тензора поляризовності, перерізів поглинання та розсіювання і частот поздовжнього та поперечного поверхневого плазмонного резонансу частинок вказаних форм. Встановлено, що положення поверхневого плазмонного резонансу суттєво залежить від аспектного відношення, коли плазмонні коливання відбуваються вздовж більшого розміру наночастинки і не залежить від аспектного відношення для плазмонних коливань вздовж меншого розміру. Показано, що положення й амплітуда максимумів перерізу поглинання залежать не лише від аспектного відношення, а і від форми поперечного перерізу частинки (коло або п'ятикутник). В свою чергу, зміна матеріалу наночастинок має наслідком лише зсув спектральних кривих зі збереженням відносних положень і величин максимумів перерізів поглинання.

Ключові слова: металева наночастинка, біконус, біпіраміда, плазмонний резонанс, поляризовність, еквівалентний сфероїд, аспектне відношення.